Synthesis and magnetic reversal of bi-conical Ni nanostructures Synthesis and magnetic reversal of bi-conical Ni nanostructures

Nicolas Biziere, R Lassalle Ballier, M.C. Clochard, M Viret, Travis L Wade, E Balanzat, Jean Eric Wegrowe

AIP | Journal of Applied Physics

Synthesis and magnetic reversal of bi-conical Ni nanostructures

N. Biziere, R. Lassalle Ballier, M. C. Clochard, M. Viret, T. L. Wade et al.

Citation: J. Appl. Phys. **110**, 063906 (2011); doi: 10.1063/1.3638072
View online: http://dx.doi.org/10.1063/1.3638072
View Table of Contents: http://jap.aip.org/resource/1/JAPIAU/v110/i6
Published by the American Institute of Physics.

Synthesis and magnetic reversal of bi-conical Ni nanostructures

N. Biziere,[1,2,a)] R. Lassalle Ballier,[3] M. C. Clochard,[1] M. Viret,[3] T. L. Wade,[1] E. Balanzat,[4] and J. E. Wegrowe[1]
[1]*Laboratoire des Solides Irradiés, CEA/CNRS/Ecole Polytechnique, Ecole Polytechnique, 91128 Palaiseau Cedex, France*
[2]*CEMES-CNRS, 29 Rue Jeanne Marvig, 31055 Toulouse, France*
[3]*Service de Physique de l'Etat Condensé, DSM/IRAMIS/SPEC, CEA Saclay URA CNRS 2464, 91191 Gif-Sur-Yvette Cedex, France*
[4]*CIMAP, Unité Mixte CEA-CNRS-ENSICAEN, F-14070 Caen Cedex 5, France*

(Received 27 May 2011; accepted 5 August 2011; published online 20 September 2011)

Template synthesis in polyethylene terephthalate (PET) membranes has been used to grow hour glass shaped nickel nanowires with a constriction in the range of tens of nanometers at the center. Anisotropic magnetoresistance measurements have been performed on a single nanowire to follow magnetization reversal of the structure. The results are explained via 3D micromagnetic simulations showing the appearance of a complex vortex state close to the constriction whose propagation depends on the angle between the cone axis and the applied field. The interest of this original growth process for spintronics is discussed. © *2011 American Institute of Physics*. [doi:10.1063/1.3638072]

I. INTRODUCTION

In the field of spintronics, magnetic nanowires are being intensively studied. Particular attention has been paid to the interplay between an electrical current or a magnetic field and a domain wall (DW). This is highly motivated by the technological potential of DWs for magnetic data storage,[1] logic gates,[2] and magnetic sensor[3] applications. For example, it has been shown that a high density spin polarized current can exert a torque on the spins of a DW via the so-called spin transfer torque (STT) and induce the motion of the DW.[4–8] Reciprocally, the nonlinear profile of the DW affects the transport properties and contributes to the magnetoresistance.[9–11] While several theories have been proposed to explain the microscopic origin of STT in DW (Refs. 12–14) or DW magnetoresistance,[15,16] some fundamental questions still remain unclear.

In order to better understand these effects, a number of experiments have been performed on patterned nanostructures with constrictions down to a few nanometers. Indeed, confinement acts as an artificial pinning site for DWs (Refs. 17 and 18) through the local modification of the magnetostatic energy. As a first approximation, the constriction can then be modeled as a pinning potential well whose amplitude and profile depend on the shape and size of the constriction and on the DW configuration. The DW can then be considered as a quasi-particle, with mass and inertia, moving in this potential well under an external force (electrical current or magnetic field). However, beside a precise knowledge of the sample geometry, it is fundamentally important to know the structure of the domain wall at the constriction (Bloch, Néel, vortex…) to get a complete description of the system. This point generally requires micromagnetic simulations or advanced imaging techniques such as MFM, Lorentz microscopy, or polarized X-ray photoemission. The shape of the nanostructure will also influence the maximum velocity at which a DW can propagate in a strip (referred to as the walker limit) and also the amplitude of the so-called intrinsic pinning.[19] Interestingly, DWs are massless in cylindrical nanowires with a suppression of the walker limit leading to very high DWs velocities.[20] This is due to the symmetry of the nanowire that prevents a modification of the internal structure of the DW during its displacement, in opposition to the case of flat strips. In this context, it is then particularly interesting to develop new techniques to grow magnetic nanostructures with original shapes and symmetries and to understand their magnetic configurations that are most often non-linear for sub-micron sizes.

In this paper, we propose to study the micromagnetic states of a single nickel nanowire with a bi-conical symmetry. One unique feature of this geometry is the possibility to get a constriction of a few tens of nanometers with a cylindrical symmetry. It has been achieved by developing an original technique based upon template synthesis in a specific matrix. The magnetic states of the nanostructure are probed via the anisotropic magnetoresistance (AMR) of the wire and explained using 3D micromagnetic simulations. We show that magnetization reversal occurs through the nucleation of a complex vortex like a state whose propagation through the constriction depends on the direction of the applied field. Moreover, AMR measurements indicate that small inhomogeneities help to trap this DW close to the constriction.

II. MATERIALS AND METHODS

Swift heavy ions (SHI) irradiations were performed using SME beam line at the GANIL (Cyclotron accelerator at Caen, France). 16 μm thick poly(ethylene terephthalate) (PET) films (from GoodFellow, kindly donated by CIMAP laboratory) were irradiated with Kr^{31+} ions of 10 Mev/amu

[a)]Electronic mail: nicolas.biziere@cemes.fr.

under helium atmosphere with fluences of 5.10^6 and 5.10^8 ions/cm^2. During SHI, ions induce a continuous trail of excitations and ionizations leading to the formation of specific cylindrical damage zones called latent tracks all along their trajectory through the thickness of PET film. The final heterogeneous solid is then formed of latent tracks (or highly damaged zones) and pristine areas. The latent tracks are more fragile than the non-irradiated bulk.

PET membrane ion tracks were then revealed by symmetrical chemical etching in 2 N NaOH at 80 °C. The conical shape of the pores is ensured by the velocity anisotropy of the hydrolysis reaction between the damage zone created during the ion bombardment and the polymer bulk. For the samples of interest here, the hydrolysis velocity of the membrane in the direction perpendicular to the surface is about 10 times faster than in the direction parallel to the surface leading to cone shaped etch tracks. This ratio is highly dependent on the NaOH concentration, temperature, and ion kinetic energy. As the dissolution by hydrolysis is performed on each side of the PET, a constriction is realized when two growing cones meet. The diameter of the constriction is mainly controlled by the time the membrane spends in the NaOH solution. All samples presented below have been grown in PET etched for 7.5 mn. Figure 1(a) shows the Field Emission Scanning Electron Microscopy (FESEM) image of the cross-section of the resulted bi-conical tracks. The flexibility of the track etching technique allows the synthesis of a wide variety of cone-shaped tracks with different constriction sizes.

Electrodeposition is then used to fill the pores with Ni. A piece of PET for which one side has been sputtered with a 150 nm gold layer is immersed into an aqueous electrolytic solution composed of $NiSO_4$ and H_3BO_4. The electric potential between the golden surface of the PET (working electrode) and an Ag/AgCl reference electrode is set to -1.000 Vs. The electrodeposition is stopped when a large sheet of Ni has grown on top of the PET. As shown by previous studies about cylindrical and cigar shaped tracks,[21] the current versus time plots during electrodeposition should reflect the pore geometry. The black curve in Fig. 2 corresponds to the electrodeposition current versus time plot for a PET membrane with a pore density of 5.10^8/cm^2. Since the electrodeposition current density is proportional to area, it is large at the beginning of the electrodeposition (about 47 mA/cm^2), corresponding the conical openings of the membranes. The current density then decreases as the nickel deposit approaches the 50 to 100 nm constriction in the middle of the membrane (about 16 mA/cm^2 at 680 s). Finally the current density increases as the deposition proceeds to the conical openings at the other side and then surface growth outside the pores. For comparison, nickel nanowires were deposited in 6 micron thick 30 nm pore diameter polycarbonate filters (Poretics) using the same electrodeposition conditions, (see Fig. 2, gray curve). The nominal interior pore diameter of the filters is about 60 nm depending on the measurement technique [see Ref. 21]. It is interesting to note that the current density for constriction is similar to that for the electrodeposition in the filter, 12–15 mA/cm^2. The pore density for the filter is $3*10^8$/cm^2 and $5*10^8$/cm^2 for the bi-cone membrane while deposition area is 9 cm^2 for filter and 6 cm^2 for the bi-cone membrane resulting in $2.7*10^9$ pores for the filter and $3.0*10^9$ for the bi-cone membrane.

To characterize the shape of the nanowires, electrodeposition in PET membrane with a pore density of 5.10^6 has been realized. Once Ni nanowires have been grown as explained above, the membrane is left in NaOH until it is completely dissolved. Ni nanowires attached to the large Ni plate can then be observed. However because of their weight, they break at the constriction during the dissolution of the membrane. Figure 1(b) is a FESEM electron microscopy image of one half of a Ni nanowire. We can clearly observe the conical shape of the wire thus validating our method. The size of the constriction for this wire is below 100 nm and the cone aperture is about 5°. We have observed on a few nanowires that the diameter at the break can range from 50 to 100 nm and that the cone angles ranges between 4 and 6°. We also observe roughness on the lateral surface of the cone that we estimate to be about 1% of the diameter.

III. AMR MEASUREMENTS

In order to measure the magnetoresistance of Ni nanowires, electrodeposition is performed in 5.10^6/cm^2 pore density PET membranes with 150 nm of gold sputtered on both

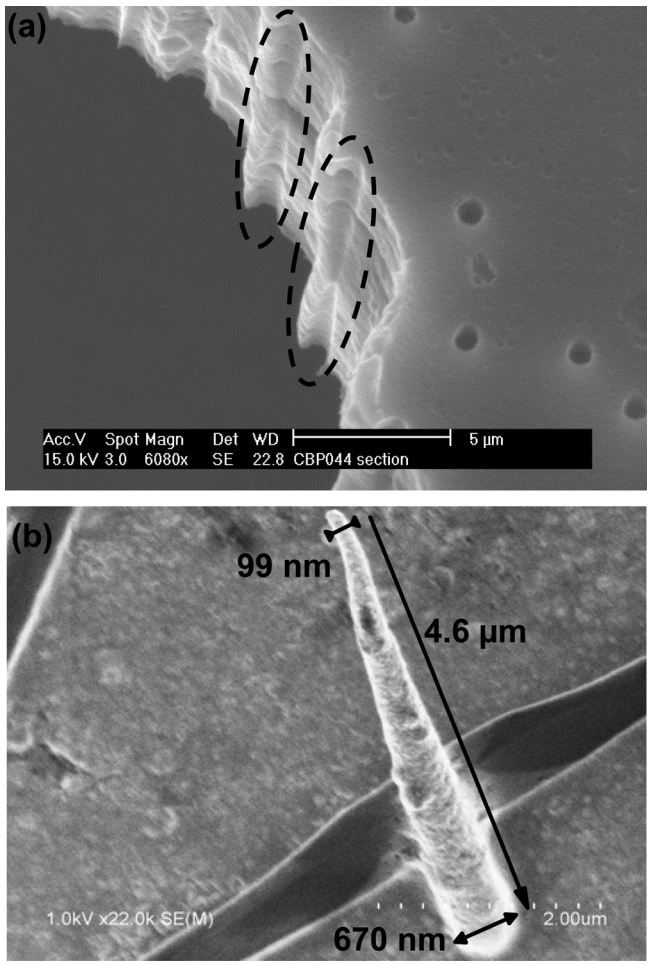

FIG. 1. (a) Electron microscopy image of the cone trace in the PET after freeze fracturing. The dotted circle is a guide to the eye to localize the cone shaped trace. (b) Electron microscopy image of half of a Ni nanowire after dissolution of the PET matrix.

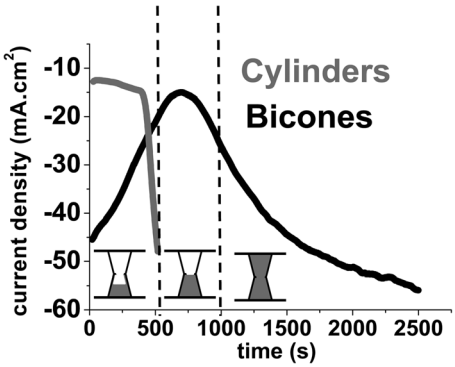

FIG. 2. Electrochemical reduction current density as a function of time for the potentiostatic plating of Ni (-1.000 V) in cylindrical pores (gray curve) and in bi-conical pores (black curve). The schematics display three different stages of the growth process corresponding to the black curve. In region I, metal wires (filled) are before the constriction, the current decreases following the surface decrease. In region II, the metal filling is at the constriction of bi-conical tracks, minimum of current intensity, and minimum exposed surface to electrolyte. In region III, growth continues to larger surfaces up to the whole membrane surface.

sides. The electrical contact on a single nanowire is ensured by *in situ* recording of the current in the electrolytic cell. Indeed, when a first nanowire reaches the top surface, it short cuts the top and bottom gold layers and induces a sharp increase of the current in the cell. Details about the growth procedure are given elsewhere.[22]

Figure 3 shows the resistance of a Ni nanowire as a function of the applied magnetic field amplitude H_0 and for different angles θ between H_0 and the nanowire axis. The field is scanned from negative to positive saturation and then back. The AMR ratio, defined by $R_{//}$-$R_{\perp}/R_{//}$ measured at saturation, is about 0.55%, which is around half of the AMR ratio that has been measured on Ni cylindrical nanowires electrodeposited in commercial polycarbonate membrane[23] (between 1 and 1.5%). The difference is due to the contact resistance between the gold layers on top of the PET and the nanowire. Because the cone angle is very small, we can consider, as a first approximation, that the current lines are parallel in the cone. The cone resistance can then be estimated to lie between 8 and 10 Ω for this sample. However, because of the cone shape, the main contribution (more than 80%) to this resistance comes mainly from the constriction and a small part on each side (few hundred of nanometers). The total resistance of the different nanowires (cone + contact resistances) we have measured range between 20 and 35 Ω, a span that can be accounted for by the difference in the contact resistance, the cone angle, and the size of the constriction. This shows that despite measurement geometry in a two point contact, we are sensitive to the AMR of the constriction.

We observe in Fig. 3 that for $\theta = 0°$, the AMR slightly increases when the field amplitude decreases. This can be accounted for the uncertainty of θ. We estimate it to be up to a few degrees due to the fact that the membrane is not perfectly flat at the surface of the sample holder and to the uncertainty on the orientation of the latter in our electromagnet. The cone shape of the wire can also explain the slight increase of the AMR. Indeed, when H_0 decreases the spins at the edge of the cone tend to align parallel to the surface and therefore to the current lines.

AMR measurements reveal different magnetic states at remanence as a function of θ. More particularly, there is a clear difference between a field applied almost parallel or almost perpendicular to the cone axis. In the latter case, the magnetic state within the constriction is non-uniform with spins aligned mainly perpendicular to the cone axis.

To get a better understanding of what happens in the vicinity of the magnetic switching, we performed magnetoresistance (MR) measurements on another sample while sweeping the field in small steps of 1 mT. The results obtained for $\theta = 0$ and 50° are presented in Fig. 4. Similar results have been obtained on other samples. Each curve is an average of over 10 scans. For convenience, both MR measurements have been normalized by the value of the resistance at saturation. While the shape of both MR cycles exhibits some differences, especially when H_0 changes its sign, some similarities can be observed. In both cases the resistance decreases before H_0 reaches zero. This is proof that the magnetic state at remanence is non-uniform for both orientations of the applied field. The resistance decrease is consistent with an AMR signature of spins, which tend to align

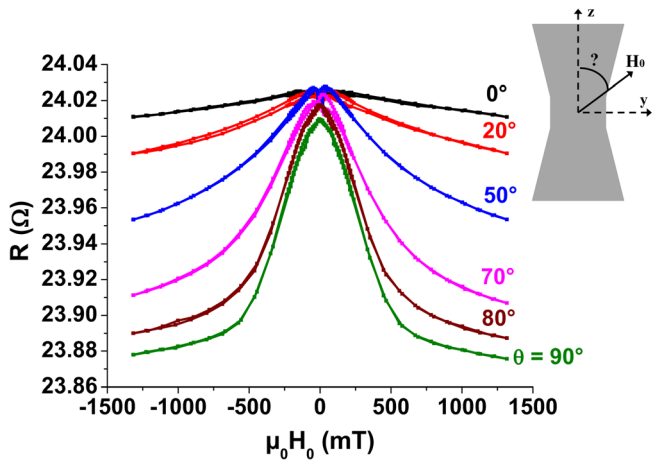

FIG. 3. (Color online) (a) MR of a single Ni nanowire as a function of the applied field H_0. Values correspond to the relative angle between H_0 and the cone axis.

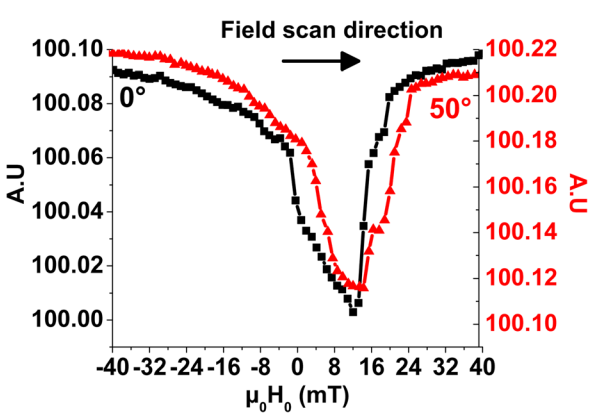

FIG. 4. (Color online) Magnetoresistance of a Ni nanowire as a function of H_0 for $\theta = 0°$ (squares) and 50° (triangles). The resistance has been normalized by the value at negative saturation for convenience.

perpendicularly to the cone axis. Then a sharp decrease of the resistance is observed at $\mu_0 H_0 = 0$ and 3 mT for $\theta = 0$ and 55°, respectively. As confirmed by the simulations (see below), we assume that this step in the resistance corresponds to the nucleation of a DW in the vicinity of the constriction. This is followed, on a field range of about 10 mT, by a slight decrease of the resistance. This can be accounted for by a small propagation of the DW. Finally, over a last range of fields of less than 10 mT and beginning at the coercive field Hc, (defined as the field for which the resistance is the lowest), the resistance increases back to its value at negative field. We note here that the difference in the switching field from one scan to another is less than 10% for both field orientations. The steps observed in this field range is a typical feature of a magnetic switching ensured by a propagating DW through the constriction hopping from one pinning site to another. It is also interesting to notice that despite the difference in θ, the values of the switching field are very similar for each orientation. This point confirms that the magnetization reversal occurs through a nucleation/propagation process instead of a coherent rotation of the spins in the constriction as one could expect from the shape anisotropy of the nanowire.

IV. MICROMAGNETIC MODELING

The 3D micromagnetic OOMMF freeware program[24] has been used to simulate the magnetic states of the cone. For obvious calculation consumption time, real samples could not be entirely simulated. Instead, the simulated wire length is taken to be 4.2 μm long, with a cone angle of 2.5°. The constriction is defined as a 100 nm long cylinder with a radius of 50 nm. On one side of the cone, we have simulated a "mushroom shaped" Ni contact. This mushroom grows at the top of the Ni nanowire during electrodeposition when the wire reaches the surface. It can be a few hundreds of nanometers up to >1 μm high depending on the sample (see Refs. 21 and 23 for more details). Here we have simulated a mushroom with a diameter of 200 nm. The parameters used for the simulations are $Ms = 4.10^5$ A/m, $A = 9.10^{-12}$ J/m. Crystalline anisotropy has been neglected because the electrodeposited Ni grows with a polycrystalline structure. The cell is a cube of 125 nm^3. Field steps have been limited to 4.5 mT in the vicinity of the switching field in order to remain within reasonable calculation times. As a first approximation the AMR of the cone can be described as the average value of the square of magnetization in the direction z of the cone axis. Figure 5 shows the result of the simulation of $\langle Mz \rangle^2$ as a function of the applied field for $\theta = 0$ and 45°. We can see that the shape is in quite good agreement with the experiments. More particularly two major features are reproduced. The first is the decrease of $\langle Mz \rangle^2$ before the field is reversed. The second is that both switching fields are quite close for both orientations of the magnetic field.

Figure 6 shows the equilibrium magnetic states calculated at the points denoted I, II, III, and IV in Fig. 5 ($\theta = 0°$). The arrows represent magnetization vectors in the xy plane for different z values. Starting from the negative saturation, two vortices appear in the mushroom and at the bottom of

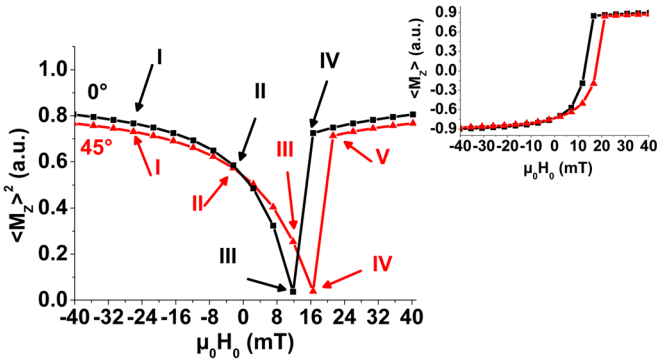

FIG. 5 (Color online) Square of the average Mz component of the magnetization of the cone for $\theta = 0°$ (squares) and 45° (triangles). Inset: Average Mz component of the magnetization for $\theta = 0°$ (squares) and 45° (triangles).

the cone thus decreasing the magnetostatic energy. The vortex in the mushroom is created around –100 mT while that at the bottom of the cone appears around −90 mT (figure not shown). We observe that the cores of the two vortices point toward the direction of the applied field (-z). However the chirality of the two vortices is opposite. We assume that the chirality of the bottom vortex is induced by the small stray field coming from the mushroom such as to close the magnetic flux outside the cone.

When decreasing the amplitude of the applied field, the vortices at top and bottom of the nanowire propagate toward the constriction (points I, II, and III) until Hc is reached. However, at point III the vortices stop at a distance of less than 1 μm from the center of the constriction in which the spins still point to the –z direction. This indicates that the cost in exchange energy to create a vortex at the center of

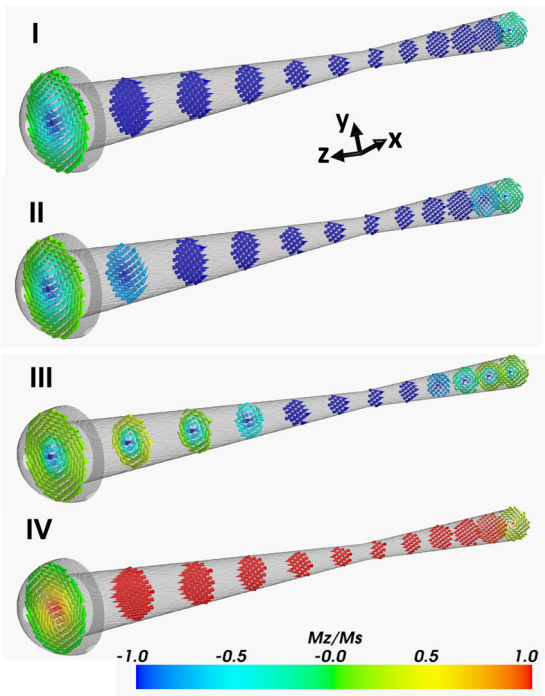

FIG. 6. (Color online) Magnetization of the cone in the xy plane at different z values. The field is applied parallel to the z axis (cone axis). The cone is preliminary saturated in the –z direction. The different images refer to the equilibrium magnetic states denoted I, II, III, and IV in Fig. 4.

the cone would be too important and that the shape anisotropy dominates. When increasing the field from III to IV the magnetization reverses in the cone. Only the vortices at the top and bottom remain but we can see that if the chirality has been conserved the core direction has been inversed to decrease the Zeeman energy. More details about the dynamic of the switching are presented below.

A similar behavior is observed for $\theta = 45°$ (field applied in the yz plane) in Fig. 7. However we observe that the chirality of the top and bottom vortices is the same at point I. This is due to the y component of the applied field, which favors a domain with a majority of spins in the –y direction when the vortex nucleate. Once again, the vortices propagate toward the constriction until the field reaches Hc for which the spins at the center of the cone are aligned in the –z direction. Unlike the case $\theta = 0°$, we observe that when the vortex propagates, the vortex core is not aligned with the axis of the cone, i.e., along the z axis, but spirals around it. We explain this fact by the competition between the Zeeman and magnetostatic energies. Indeed, at zero field the vortex core is located in the middle of the xy plane as could be expected. Then when the field is reversed, the +y component of the applied field induces a displacement of the vortex core toward the edge of the cone. However, because of the cone shape, this would push the core's magnetization to point out of the cone and induce a stray field. To allow for the magnetic flux to stay in the cone and to minimize the Zeeman energy, the vortex core spirals around the z axis so that most of the spins can rotate in the y and z directions. One important feature revealed by these simulations is that magnetic states with vortices of similar chirality on each side of the constriction are more stable.

To explain the dynamics of the switching we present in Fig. 8 some snapshots of the magnetization for $\theta = 0°$ starting from point III and before it reaches the equilibrium position of point IV. Similarly to the case at $\theta = 45°$, we observe that the vortex core begins to spiral around the z axis to minimize the Zeeman energy. We emphasize here that this spiral is an unstable state unlike at point III for $\theta = 45°$. Then in a small zone in each side of the cone, we observe a flip of the vortex core to allow for the spins to align in the direction of the applied field. Then this domain grows and pushes away the vortices toward the top and bottom of the structure. We can notice that the spins flip first in the top part of the cone for which the vortex has entered the furthest in the cone. At this step a uniform domain with the spins aligned in the opposite direction of the field is trapped in the constriction. The vortices act as a head-to-head and a tail-to-tail domain wall as schematically shown by the arrows. Finally the switching is achieved when the two vortices coming from each part of the cone annihilate in the constriction.

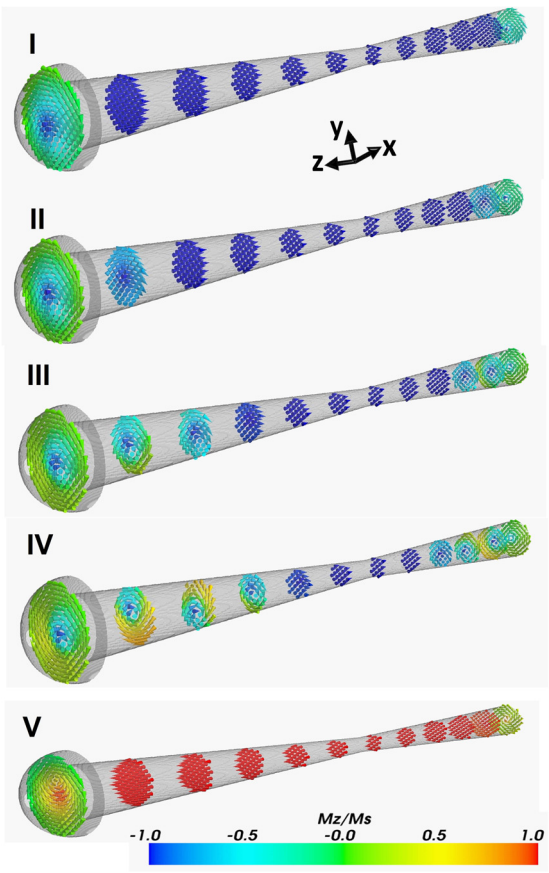

FIG. 7. (Color online) Magnetization of the cone in the xy plane at different z values. The field is applied at 45° from the z axis in the yz plane. The cone is preliminary saturated with a negative field with respect to the axis orientation. The different images refer to the equilibrium magnetic states denoted I, II, III, IV, and V in Fig. 4.

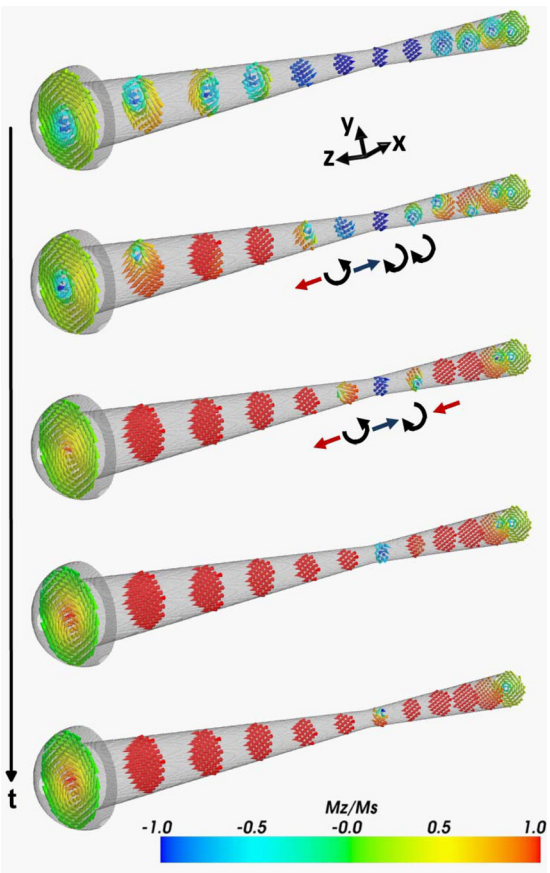

FIG. 8. (Color online) Snapshots of the magnetization in the xy plane at different z values during switching for $\theta = 0°$. Arrows are a schematic of the magnetization in the vicinity of the constriction.

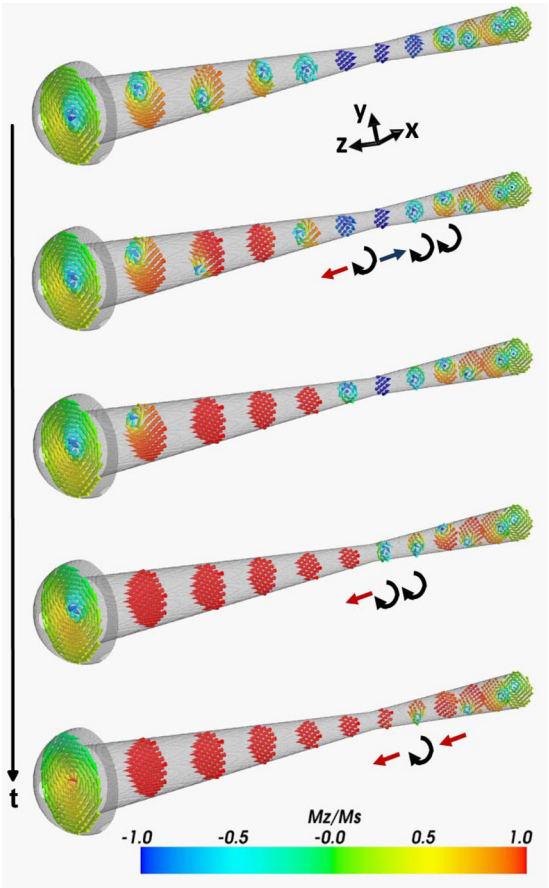

FIG. 9. (Color online) Snapshots of the magnetization in the xy plane for different z values during switching for $\theta = 45°$. Arrows are a schematic of the magnetization in the vicinity of the constriction.

The situation for $\theta = 45°$ is slightly different as can be observed in Fig. 9. Indeed the magnetization flips only in the part of the cone with the mushroom. Then we see that the vortex can propagate easily through the constriction. The reason is that the magnetic domain with spins aligned in the –z direction is not held on each side by two domains with spins in the +z direction and so it does not prevent the vortex to enter the constriction.

It is interesting to compare the magnetic simulations with the AMR experiments. Indeed, simulations performed on an ideal system with no roughness highlight that the vortices propagate through the constriction without being trapped. While it is difficult to know the exact diameter of the constriction and the cone angle of the sample we measured, we can assume that micromagnetic mechanisms of switching are most likely equivalent for similar cone angles and similar constriction diameters. Then we can assume that the steps observed in the AMR in Fig. 3 for $H_0 < Hc$ correspond to local roughness induced pinning of the vortex while propagating toward the constriction. More interestingly, we can assume that the steps observed when passing Hc correspond to the pinning of the vortex in the vicinity of the constriction. Then this system becomes very interesting for spintronic studies since one can trap a head to head or tail to tail vortex domain wall in a constriction with cylindrical symmetry.

V. CONCLUSIONS

We have developed an original method based upon template synthesis in a PET matrix to grow bi-conical Ni nanowires with a constriction of a few tens of nanometers. The micromagnetic states of a single nanowire have been studied through AMR and micromagnetic modeling during magnetization reversal. Simulations have revealed a complex vortex like state whose propagation through the constriction depends on the relative angle between the applied field and the cone axis. While simulations predict no pinning of the vortex in the constriction, our magnetoresistance measurements provide evidence that small inhomogeneities allow the trapping of head-to-head or tail-to-tail domain walls in the vicinity of the constriction.

[1]S. S. P. Parkin, M. Hayashi, and L. Thomas, Science **320**, 190 (2008).
[2]J. Jaworowicz, N. Vernier, J. Ferre, A. Maziewski, D. Stanescu, D. Ravelosona, A. S. Jacqueline, C. Chappert, B. Rodmacq, and B. Dieny, Nanotechnology **20**, 215401 (2009).
[3]G. A. Wang, Y. Masuda, T. Kato, and S. Iwata, J. Phys. D: Appl. Phys. **43**, 455001 (2010).
[4]S. Emori and G. S. D. Beach, Appl. Phys. Lett. **98**, 132508 (2011).
[5]X. Jiang, L. Thomas, R. Moriya, and S. S. P. Parkin, Nano Lett. **11**, 96 (2011).
[6]J.-Y. Chauleau, R. Weil, A. Thiaville, and J. Miltat, Phys. Rev. B **82**, 214414 (2010).
[7]X. Waintal and M. Viret, Europhys. Lett. **65**, 427 (2004).
[8]J. Heinen, O. Boulle, K. Rousseau, G. Malinowski, M. Kläui, H. J. M. Swagten, B. Koopmans, C. Ulysse, and G. Faini, Appl. Phys. Lett. **96**, 202510 (2010).
[9]A. K. Patra, A. von Bieren, S. Krzyk, J. Rhensius, L. J. Heyderman, R. Hoffmann, and M. Kläui, Phys. Rev. B **82**, 134447 (2010).
[10]C. H. Marrows, Adv. Phys. **54**, 585 (2005).
[11]J. L. Prieto, M. G. Blamire, and J. E. Evetts, Phys. Rev. Lett. **90**, 027201 (2003).
[12]G. Tatara and H. Kohno, Phys. Rev. Lett. **92**, 086601 (2004).
[13]A. Vanhaverbeke and M. Viret, Phys. Rev. B **75**, 024411 (2007).
[14]L. Berger, Phys. Rev. B **80**, 144427 (2009).
[15]L. Berger, Phys. Rev. B **75**, 174401 (2007).
[16]M. Viret, D. Vignoles, D. Cole, J. M. D. Coey, W. Allen, D. S. Daniel, and J. F. Gregg, Phys. Rev. B **53**, 8464 (1996); P. M. Levy and S. Zhang, Phys. Rev. Lett. **79**, 5110 (1997).
[17]J.-S. Kim, O. Boulle, S. Verstoep, L. Heyne, J. Rhensius, M. Kläui, L. J. Heyderman, F. Kronast, R. Mattheis, C. Ulysse, and G. Faini, Phys. Rev. B **82**, 104427 (2010).
[18]A. Bisig, J. Rhensius, M. Kammerer, M. Curcic, H. Stoll, G. Schütz, B. Van Waeyenberge, K. W. Chou, T. Tyliszczak, L. J. Heyderman, S. Krzyk, A. von Bieren, and M. Kläui, Appl. Phys. Lett. **96**, 152506 (2010).
[19]T. Koyam, Nature Mater. **10**, 194 (2011).
[20]M. Yan, A. Kakay, S. Gliga, and R. Hertel, Phys. Rev. Lett. **104**, 057201 (2010).
[21]C. Schönenberger, B. M. I. van der Zande, L. G. J. Fokkink, M. Henny, C. Schmid, M. Krüger, A. Bachtold, R. Huber, H. Birk, and U. Staufer, J. Phys. Chem. B **101**, 5497 (1997).
[22]J. E. Wegrowe, Q. A. Nguyen, and T. L. Wade, IEEE Trans. Mag. **46**, 3 (2010).
[23]J.-E. Wegrowe, Q. A. Nguyen, M. Al-Barki, J.-F. Dayen, T. L. Wade, and H.-J. Drouhin, Phys. Rev. B **73**, 134422 (2006).
[24]M. J. Donahue and D. G. Porter, OOMMF User's Guide, http://math.nist.gov/oommf.